

Analytical Model of an Eddy Current Retarder with Consideration of Nonlinear Magnetization Characteristics of its Ferromagnetic Material

Seongyun Park, Kyihwan Park

School of Mechatronics
Gwangju Institute of Science and Technology
Gwangju, Republic of Korea
baksg@gist.ac.kr, khpark@gist.ac.kr

Changhee Yoo, Jungkyu Hwang

Advanced Development Team
Sangsin Brake Co., Ltd.
Daegu, Republic of Korea
yooch@sangsin.com, teriushjg@sangsin.com

Abstract—The nonlinearity magnetization characteristics of the rotor material is a problem in the analysis of eddy current retarders (ECR) because the typical operating conditions of ECRs require high supplied currents. In order to address the nonlinearity of the rotor material, a proper method is needed. In this paper, we propose a process to express the effective magnetic flux considering the nonlinear magnetization characteristics of the ferromagnetic materials used in ECRs. Using a numerical iterative scheme to deal with nonlinear magnetization characteristics, we explain why the torque tends to increase less with higher supplied currents. Using the nonlinear analysis model, we discuss the effects of several design parameters on the torque-speed behavior in order to determine the parameters that are most important for torque-speed performance.

Keywords—Eddy current retarder, Nonlinear magnetization characteristics, Magnetic saturation, Numerical analysis, Copper layer.

I. INTRODUCTION

With stricter safety regulations being imposed on large vehicles, there is an increasing demand for velocity retarders, which assist the primary friction brakes. In fact, the use of retarders for heavy-duty vehicles is a growing trend in Japan, Australia, Europe, and North America. Among several types of retarders, ECRs are preferred owing to their fast response time and the small installation space they require.

ECRs are classified into linear types, drum types, and disk types, depending on their rotor shapes, and into permanent magnet types and electromagnet types, depending on their flux supply sources. For permanent-type ECRs, the path of the magnetic flux through the rotor is controlled by mechanically moving the magnets, which alters the polarity between adjacent magnets. Although this type of retarder requires no external power source, it is mechanically complex and suffers from off-state leakage flux [1]. Electromagnet-type ECRs, on the other hand, in which the magnetic flux is controlled by a coil current, are mechanically simple and free from flux leakage.

The approach to analyze an ECR can be classified into Finite Element Method (FEM) [2-4] and analytical method [5-10]. Research on ECRs by FEM has mostly been conducted on industrial applications with high torques. Jang analyzed a linear-type ECR with a permanent magnet array

using [2]. Choi discussed an optimum method for managing a Halbach array using FEM, as well for linear rotor-type ECRs [3]. For a drum-type ECR with permanent magnets, Alvaro took into consideration the thermal effect [4]. The merit of FEM analysis is the accuracy of its solution. However, the downside of FEM is a long computation time for even moderately complex geometry.

Without recourse to FEM analysis, analytical methods have been utilized to model the eddy current distribution and retarding torque of ECRs. The advantage of analytical methods over FEM is the reduced computation time and increased understanding of physical principles underlying the ECR. Smythe studied the effects of an induced magnetic flux on the retarding behavior [5]. Schieber analyzed the distribution of eddy currents in the vicinity of pole arrays using the magnetic vector potential [6]. By assuming constant power dissipation for all speed regions, Wouterse showed that the retarding force can be described in terms of the air gap and pole diameter [7]. Lee proposed a model by using an image charge method for a disk-type ECR [8]. A representative analytical model was proposed by Davies, who derived the torque equation from a diffusion equation of the eddy current density in a three-dimensional Cartesian coordinate system [9]. By applying the energy conservation, Malti derived a torque equation in three-dimensional cylindrical coordinates [10].

However, the problem of the analytical approaches is that an enormous deviation of the theoretical from the experimental result is produced when a high current is applied to the electromagnets of the ECR. The discrepancy is due to the fact that the magnetic flux density does not increase linearly with the coil current. The approach in this paper to address this difficulty is to find the effective magnetic density by calculating iteratively using the magnetization data of the rotor material.

Section II is devoted to explanation on the configuration of a drum-type ECR. The analytical procedure combined with iteration method is explained in Section III through V. In Section III, the eddy current density equation is derived. Section IV is divided by two parts. In Part A, the magnetic circuit is utilized to obtain an expression for the effective magnetic flux density. Part B explains the iteration steps to compute the effective magnetic flux. After that, Section V derives the torque equation by applying the Lorentz force formula. In result and discussion, the analytical and

experimental results are compared, and the effects of some design variables on the torque-speed characteristics are evaluated.

II. CONFIGURATION AND PRINCIPLE OF A DRUM-TYPE ECR

Fig. 1 shows the structure and actual shape of the rotor and stator for the drum-type ECR that was studied in the present work. As shown in Fig. 2, the ECR is mounted at the end of a propeller shaft in a vehicle.

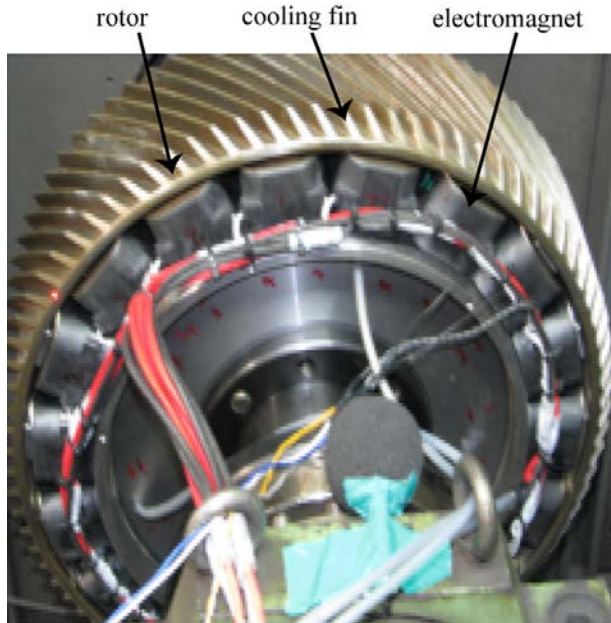


Figure 1. Configuration of drum-type ECR.

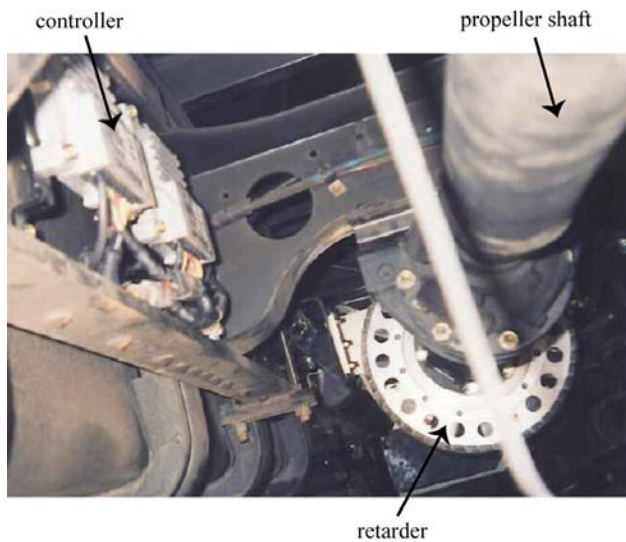


Figure 2. ECR mounted in a vehicle.

A pair of electromagnets was used to supply the magnetic flux in the radial direction through the rotor. Nine pairs of electromagnets were used to produce a peak torque of 800 N·m at a maximum current. The fins on the outer surface of the rotor dissipated the heat generated by the eddy current. The torque is controlled by varying the amount of coil current supplied from the retarder controller. A maximum current of 72 A can be supplied to 18 electromagnets.

The eddy current generated in the moving rotor and the applied magnetic flux interact to produce a force that opposed the direction of rotation, attributed to Faraday's law. In the next session, the physical model of an ECR is developed based on fundamental electromagnetic equations.

III. DERIVATION OF EDDY CURRENTS IN THE ROTOR

Table 1 lists the definitions of the design parameters and material properties. Fig. 3 shows the front, side, and isometric views of one pair of the electromagnets and the corresponding portion of the rotor. The rotor is usually made of steel to ensure its high stiffness. The surface of the rotor is coated with copper in order to generate a large amount of eddy current, because copper has a higher conductivity than steel. In this work, the permeability and conductivities of the steel and copper are considered separately in order to analyze the effect of the copper coating thickness on the generation of the eddy current.

TABLE I. DEFINITION OF THE DESIGN PARAMETERS AND MATERIAL PROPERTIES

Symbol	Physical property
μ_1, μ_2	permeability (N·A ²)
r_1, r_2	resistivity ($\Omega\cdot\text{m}$)
g	airgap (mm)
λ	pole pitch (mm)
d	depth of copper plating (mm)
L	axial length of rotor (mm)
L_a	axial length of pole (mm)
L_b	pole width (mm)
D	rotor diameter (mm)
p	number of pole pairs

The distribution of eddy current density is described by (1), which is obtained using Faraday's law, Ampere's law, and Ohm's law [9].

$$\nabla^2 \mathbf{J} = \frac{\mu}{\rho} \frac{\partial \mathbf{J}}{\partial t} \quad (1)$$

Since we know that there is no eddy current density in the z direction at the edges of the rotor, there is no eddy current in the x direction at the center line of rotor. Hence, we have boundary conditions of

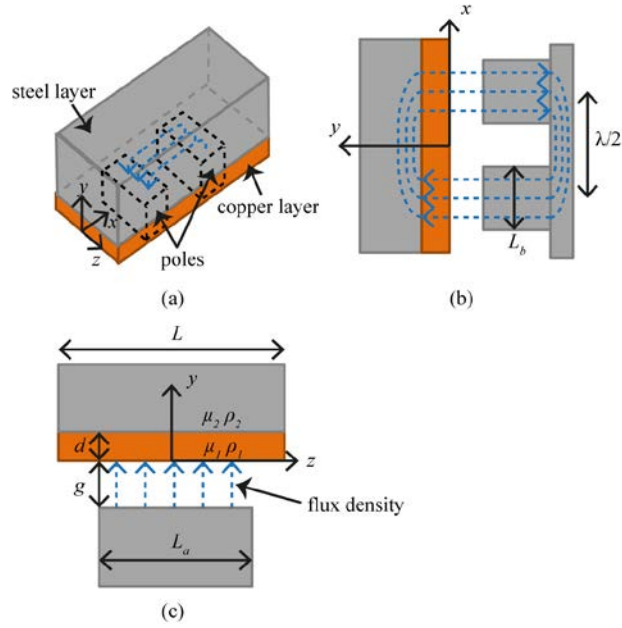


Figure 3. One pair of the electromagnets and corresponding portion of the rotor: (a) Isometric view, (b) side view, and (c) front view.

$$\begin{aligned} J_{z,copper}(z=L/2) &= 0, J_{x,copper}(z=0) = 0, \\ J_{z,steel}(z=L/2) &= 0, J_{x,steel}(z=0) = 0. \end{aligned} \quad (2)$$

From the electric field boundary condition of $E_{z,steel} = E_{z,copper}$ and by using $\mathbf{E} = \rho\mathbf{J}$, we obtain

$$\rho_1 J_{z,copper} = \rho_2 J_{z,steel}. \quad (3)$$

From the magnetic field boundary condition of $H_{z,steel} = H_{z,copper}$ and by using $\nabla \times \mathbf{J} = -\frac{\mu}{\rho} \frac{\partial \mathbf{H}}{\partial t}$, we obtain

$$\frac{\rho_1}{\mu_1} \frac{\partial J_{x,copper}}{\partial y} = \frac{\rho_2}{\mu_2} \frac{\partial J_{x,steel}}{\partial y}. \quad (4)$$

Then, using (1), (2), (3), and (4), we obtain the eddy current density in the copper-and-steel layer [9] as follows:

$$\begin{aligned} J_{x,copper} &= \text{Re} \frac{\lambda}{2L} e^{j(n(2\pi y/\lambda - \omega t) - \pi/2)} \left\{ \frac{e^{\gamma_{1mn}(2d-y)} + e^{\gamma_{1mn}y}}{1 + e^{2\gamma_{1mn}d}} \right\} \frac{m}{n} \hat{J}_{mn} \sin \frac{m\pi z}{L}, \\ J_{z,copper} &= \text{Re} e^{j(n(2\pi y/\lambda - \omega t))} \left\{ \frac{e^{\gamma_{1mn}(2d-y)} + e^{\gamma_{1mn}y}}{1 + e^{2\gamma_{1mn}d}} \right\} \hat{J}_{mn} \cos \frac{m\pi z}{L}, \\ J_{x,steel} &= \text{Re} \frac{\rho_1}{\rho_2} \frac{\lambda}{2L} e^{j(n(2\pi y/\lambda - \omega t) - \pi/2)} \left\{ \frac{2e^{\gamma_{1mn}d}}{1 + e^{2\gamma_{1mn}d}} \right\} e^{\gamma_{2mn}(d-y)} \frac{m}{n} \hat{J}_{mn} \sin \frac{m\pi z}{L}, \\ J_{z,steel} &= \text{Re} \frac{\rho_1}{\rho_2} e^{j(n(2\pi y/\lambda - \omega t))} \left\{ \frac{2e^{\gamma_{1mn}d}}{1 + e^{2\gamma_{1mn}d}} \right\} e^{\gamma_{2mn}(d-y)} \hat{J}_{mn} \cos \frac{m\pi z}{L}. \end{aligned} \quad (5)$$

where \hat{J}_{mn} is the magnitude of the eddy current, and γ_{2mn} and γ_{1mn} are defined as

$$\begin{aligned} \gamma_{1mn}^2 &= \left(\frac{2n\pi}{\lambda} \right)^2 + \left(\frac{m\pi}{L} \right)^2 + j\omega n \frac{\mu_1}{\rho_1}, \\ \gamma_{2mn}^2 &= \left(\frac{2n\pi}{\lambda} \right)^2 + \left(\frac{m\pi}{L} \right)^2 + j\omega n \frac{\mu_2}{\rho_2}. \end{aligned} \quad (6)$$

IV. THEORETICAL MAGNETIC CIRCUIT MODEL FOR THE PROPOSED ECR

Let us assume that the eddy current density \mathbf{J} and effective magnetic flux density \mathbf{B}_e are generated when the rotor is in motion. We then have Faraday's law as

$$\rho(\nabla \times \mathbf{J}) = -\frac{\partial \mathbf{B}_e}{\partial t}. \quad (7)$$

By inserting $J_{x,copper}$, $J_{z,copper}$ into (7), we obtain the effective magnetic flux density in the y direction, B_{ey} , as

$$\begin{aligned} B_{ey}(x, y, z, t) &= -\int \rho_1 \left(\frac{\partial J_{x,copper}}{\partial z} - \frac{\partial J_{z,copper}}{\partial x} \right) dt \\ &= \text{Re} e^{jn(2\pi y/\lambda - \omega t)} \hat{B}_{mn} \left\{ \frac{e^{\gamma_{1mn}(2d-y)} + e^{\gamma_{1mn}y}}{1 + e^{2\gamma_{1mn}d}} \right\} \cos \frac{m\pi z}{L}. \end{aligned} \quad (8)$$

where \hat{B}_{mn} represents the amplitude of the effective flux density [9] and is defined as

$$\hat{B}_{mn} = -\frac{2\pi\rho_1}{\lambda\omega} \hat{J}_{mn} \left\{ 1 + \left(\frac{m\lambda}{2nL} \right)^2 \right\}. \quad (9)$$

\hat{B}_{ey} is an essential variable in the eddy current analysis in this work, since it is ultimately used for calculating the retarding torque.

A. Magnetomotive relationship used for obtaining amplitude of effective flux density

As can be seen in (8), \hat{B}_{ey} can be obtained only if \hat{B}_{mn} is correctly calculated. The other parameters such as λ , ω , d , γ_1 , and γ_2 can be easily obtained from the mechanical specifications of the retarder. For this purpose, we will consider the relationships associated with the magnetic circuit, which is composed of a pair of poles and a rotor, as shown in Fig. 4(a).

From the magnetic circuit model shown in Fig. 4(b), we obtain the first relationship as

$$\mathbf{F}_{sy}(0, 0, 0, t) = \mathbf{F}_{iy}(0, 0, 0, t) + \mathbf{F}_{ey}(0, 0, 0, t) \quad (10)$$

where \mathbf{F}_{sy} is the supplied magnetomotive force produced by the supplied current, \mathbf{F}_{iy} is the induced magnetomotive force produced by the eddy current, and \mathbf{F}_{ey} is the effective magnetomotive force.

Equation (10) is obtained from the magnetic circuit, as shown in Fig. 4(b). In Fig. 4(b), Φ_{ey} and R are the effective magnetic flux and the effective reluctance, respectively. We obtain \mathbf{F}_{sy} , \mathbf{F}_{iy} , and \mathbf{F}_{ey} as follows:

1) Supplied magnetomotive force

If we assume that the supplied magnetomotive force $\mathbf{F}_{sy}(x, 0, z, t)$ has a constant value of Ni above the pole area and 0 elsewhere, we can describe $\mathbf{F}_{sy}(x, 0, z, t)$ as a Fourier series as

$$\mathbf{F}_{sy}(x, 0, z, t) = Ni \operatorname{Re} \sum_{n=1,3,\dots} C_n e^{j\left(n\left(\frac{2\pi x}{\lambda} - \omega t\right) - \frac{n\pi L_a}{\lambda} - n\phi\right)} \sum_{m=1,3,5,\dots} C_m \cos \frac{m\pi z}{L} \quad (11)$$

where, $C_m = \frac{4}{m\pi} \sin\left(\frac{m\pi L_a}{2L}\right)$ and $C_n = \frac{4}{n\pi} \sin\left(\frac{n\pi L_b}{\lambda}\right)$ represent the coefficients of a Fourier series for a square wave, and ϕ is the phase delay with respect to the effective magnetomotive force.

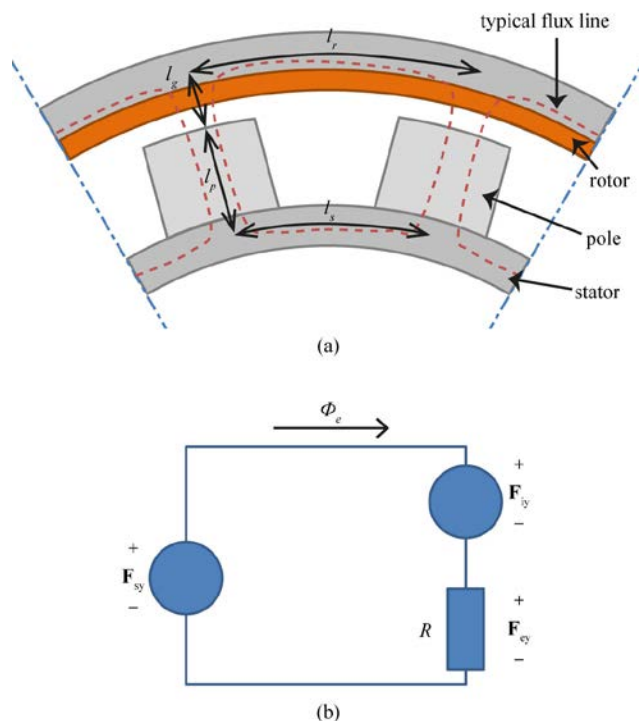


Figure 4. (a) Magnetic flux path of the ECR and (b) diagram of its magnetic circuit showing the relationship between magnetomotive forces.

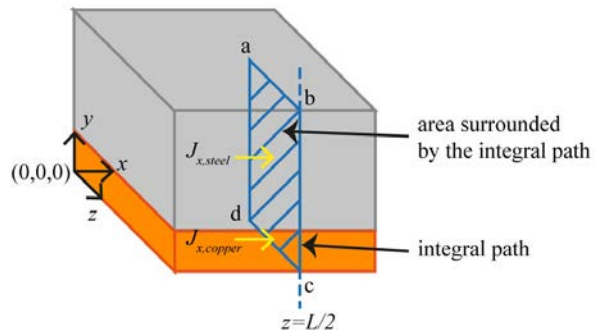


Figure 5. Rotor segment with eddy current density vectors indicated.

At $x = y = z = 0$, \mathbf{F}_{sy} is

$$\mathbf{F}_{sy}(0, 0, 0, t) = Ni \sum_{n=1,3,\dots} \sum_{m=1,3,5,\dots} C_n C_m \cos\left(n\omega t + \frac{n\pi L_b}{\lambda} + n\phi\right) \quad (12)$$

2) Induced magnetomotive force

Fig. 5 shows a rotor segment with eddy current density vectors indicated as $J_{x,copper}$ and $J_{x,steel}$. As $J_{x,copper}$ and $J_{x,steel}$ flow through the area enclosed by the integral path "abcd," the induced magnetomotive force $\mathbf{F}_{iy}(x, 0, z, t)$ can be calculated as

$$\mathbf{F}_{iy}(x, 0, z, t) = \int_{z=z}^L \int_{y=0}^d J_{x,copper} dy dz + \int_{z=z}^L \int_{y=d}^{\infty} J_{x,iron} dy dz \quad (13)$$

By inserting $J_{x,copper}$, $J_{x,iron}$ from (5) and $x = z = 0$ into (13), we obtain

$$\mathbf{F}_{iy}(0, 0, 0, t) = \sum_n \sum_{m=1,3,5,\dots} \hat{B}_{mn} \frac{\lambda^2 \omega C_m}{4\pi^2 n \rho_1} \frac{d + \frac{\rho_1}{\sqrt{2\rho_2 \alpha_{2n}}}}{1 + \left(\frac{m\lambda}{2nL}\right)^2} \cos\left(n\omega t + \frac{\pi}{2}\right) \quad (14)$$

3) Effective magnetomotive force

The effective magnetomotive force $\mathbf{F}_{ey}(0, 0, 0, t)$ can be expressed using the effective magnetic reluctance R and effective magnetic flux Φ_{ey} as

$$\mathbf{F}_{ey}(0, 0, 0, t) = R\Phi_{ey} = RA_p B_{ey} = RA_p \hat{B}_{mn} \cos(n\omega t) \quad (15)$$

where A_p is the pole area.

From (12), (14), and (15), the phase relationship among magnetomotive forces can be represented as shown in Fig. 6. We note that \mathbf{F}_{ey} leads \mathbf{F}_{iy} by a phase angle of 90° . Hence, by applying the Pythagorean theorem to the rectangular triangle composed of \mathbf{F}_{sy} , \mathbf{F}_{ey} , and \mathbf{F}_{iy} , we obtain the following relationship:

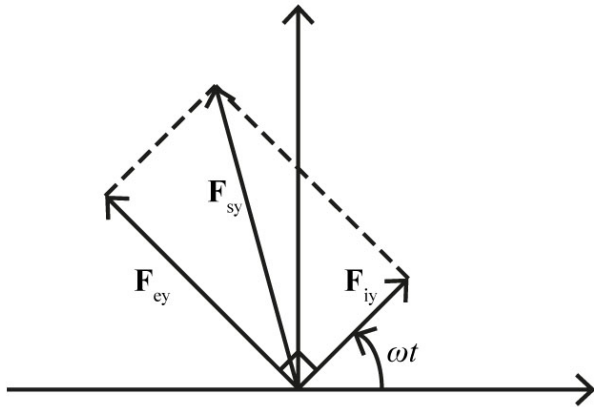


Figure 6. Phasor diagram of magnetomotive forces with phase relationships.

$$\hat{B}_{mn}^2 = \frac{(NiC_n C_m)^2}{(RA_p)^2 + \left\{ \frac{\lambda^2 \omega C_m}{4\pi^2 n \rho_1} \frac{d + \frac{\rho_1}{\sqrt{2\rho_2 \alpha_{2n}}}}{1 + \left(\frac{m\lambda}{2nL}\right)^2} \right\}^2}. \quad (16)$$

By using (16) [9], the effective magnetic flux density can be calculated.

B. Ampere's law used for obtaining the amplitude of the effective flux density

Since R is unknown in (16), as well as \hat{B}_{mn} , we need another relationship in order to obtain \hat{B}_{mn} . For this purpose, we apply Ampere's law $Ni = \oint H dl$ to the magnetic flux path, which is denoted by a dashed line in Fig. 4(a). As a result, we obtain

$$|\mathbf{F}_{ey}| = 2H_p l_p + 2H_g l_g + H_r l_r + H_s l_s \quad (17)$$

where l_p, l_g, l_r , and l_s are the flux paths, as shown in Fig. 4(a).

Using the constitutive relationship $B = \mu H$, (17) can be represented in terms of the magnetic reluctance R and magnetic flux Φ_e as

$$\begin{aligned} |\mathbf{F}_{ey}| &= 2 \frac{l_p}{\mu_p} B_p + 2 \frac{l_g}{\mu_g} B_g + \frac{l_r}{\mu_r} B_r + \frac{l_s}{\mu_s} B_s \\ &= (R_p + R_g + R_r + R_s) \Phi_e = R \Phi_e. \end{aligned} \quad (18)$$

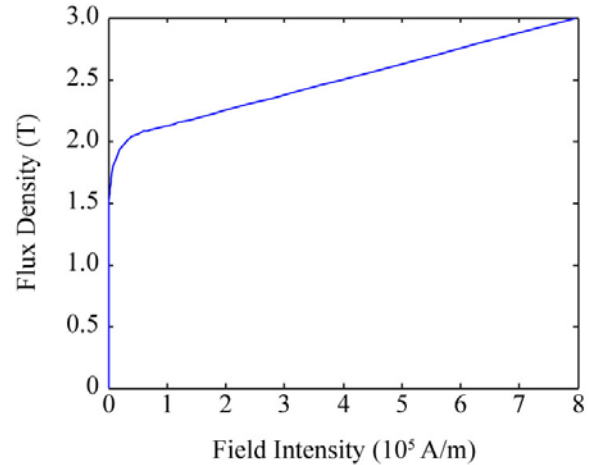


Figure 7. Magnetization curve for the rotor and stator.

Here, $R_p = \frac{2l_p}{A_p \mu_p}$, $R_g = \frac{2l_g}{A_p \mu_0}$, $R_r = \frac{l_r}{A_r \mu_r}$, and $R_s = \frac{l_s}{A_s \mu_s}$ are the reluctance of the pole, the rotor, and the stator, where A_p , μ_p , A_r , μ_r , A_s , and μ_s denote the areas and the permeability of the pole, the rotor, and the stator, respectively.

Since R_p , R_r , and R_s are negligible owing to the high relative permeability of the rotor and the pole, R becomes R_g if the rotor material is assumed to have a linear magnetization characteristic. By substituting the simplified reluctance into (16), we obtain \hat{B}_{mn} as

$$\hat{B}_{mn}^2 = \frac{(NiC_n C_m)^2}{(R_g A_p)^2 + \left\{ \frac{\lambda^2 \omega C_m}{4\pi^2 n \rho_1} \frac{d + \frac{\rho_1}{\sqrt{2\rho_2 \alpha_{2n}}}}{1 + \left(\frac{m\lambda}{2nL}\right)^2} \right\}^2}. \quad (19)$$

Given that \hat{B}_{mn} is obtained by (19), B_{ey} is also obtained by (8).

In practice, however, R is not analytically determined because the steel that composes the rotor and the stator exhibits a nonlinear magnetization characteristic for a flux density of around 1.5 T, as shown in Fig. 7. This means that \hat{B}_{mn} cannot be analytically by (19), in which a linear magnetization characteristic is assumed. To address this difficulty, we solve (16) and (21) simultaneously, with the help of the numerical method given in the following description.

- We assume an initial value for \hat{B}_{mn} . From this value, $|\mathbf{F}_{iy}|$ and $|\mathbf{F}_{ey}|$ are obtained using (14) and (15).

- Since the magnetic flux Φ_e is generated by $|\mathbf{F}_{ey}|$, we can use (17) and check the equality using the magnetization curve shown in Fig. 7 and using the relationships

$$B_p = \frac{\Phi_e}{A_p}, B_g = \frac{\Phi_e}{A_p}, B_r = \frac{\Phi_e}{A_r}, B_s = \frac{\Phi_e}{A_s}. \text{ Until}$$

both sides of (17) become the same, Φ_e keeps increased slightly. The final value of Φ_e is a numerical solution of the magnetic flux generated by $|\mathbf{F}_{ey}|$. We then have

$$\hat{B}_{mn}' = \frac{\Phi_e}{A_p}. \quad (20)$$

- Check whether the calculated solution \hat{B}_{mn}' is the same as the assumed value of \hat{B}_{mn} . When they are different, increase \hat{B}_{mn} slightly and repeat the above process, beginning with 1), until the calculated value \hat{B}_{mn}' becomes the same as the assumed value \hat{B}_{mn} . The final value \hat{B}_{mn} obtained in this iterative process is the numerical solution of the effective magnetic flux density.

Similar to the linear case, since \hat{B}_{mn} has been obtained, B_{ey} can be obtained using (8).

V. RETARDING TORQUE OF THE ECR

Fig. 8 shows the infinitesimally small volume in which B_{ey} and J_z interact. The Lorentz force F_x is obtained via the cross product of $J_z \times B_{ey}$. The eddy current retarding torque T is calculated by integrating the cross product of F_x and the distance from the center to the point of action $\frac{D}{2} + y$ over the entire rotor volume. Therefore, the total retarding torque is a summation of the torque generated at copper, T_{copper} , and the torque generated at steel, T_{steel} , as follows:

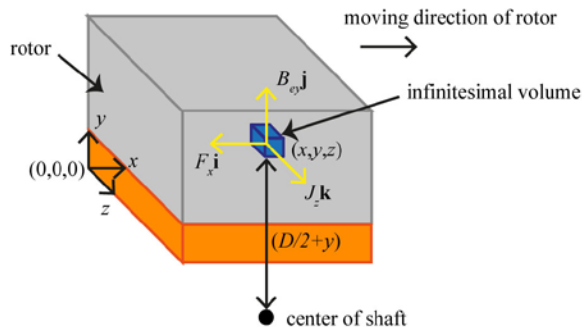


Figure 8. Lorentz force acting on the infinitesimal volume of the rotor.

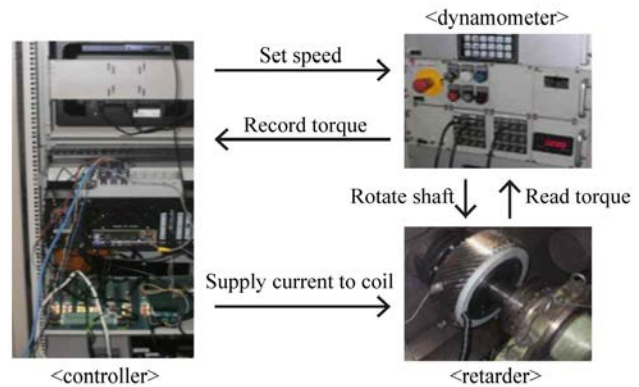


Figure 9. Schematic diagram of experimental setup.

$$T_{copper} = \sum_n \sum_m \frac{n\omega}{2\pi} \int_{x=0}^{p/2n} \int_{y=0}^d \int_{z=-l/2}^{l/2} \int_{r=0}^{2\pi/n\omega} (J_{z,copper})(B_{ey,copper}) \left(y + \frac{D}{2}\right) dx dy dz dt \quad (21)$$

$$= -\sum_n \sum_m \frac{dLp^2\lambda^3\omega C_n^2 C_m^2}{16\pi^2 \rho_1} \hat{B}_{mn}^2 \left\{1 + \left(\frac{m\lambda}{2nL}\right)^2\right\}^{-1},$$

$$T_{steel} = \sum_n \sum_m \frac{n\omega}{2\pi} \int_{x=0}^{p/2n} \int_{y=0}^d \int_{z=-l/2}^{l/2} \int_{r=0}^{2\pi/n\omega} (J_{z,steel})(B_{ey,steel}) \left(y + \frac{D}{2}\right) dx dy dz dt \quad (22)$$

$$\cong -\sum_n \sum_m \frac{p^2\lambda^3\omega LC_n^2 C_m^2}{32\pi^2 \alpha_{2n} \rho_2} \hat{B}_{mn}^2 \left\{1 + \left(\frac{m\lambda}{2nL}\right)^2\right\}^{-1},$$

$$T = T_{copper} + T_{steel} = -\sum_n \sum_m \frac{p^2\lambda^3\omega LC_n^2 C_m^2}{16\pi^2 \rho_1} \hat{B}_{mn}^2 \frac{\left\{d + \rho_1 / 2\rho_2 \alpha_{2n}\right\}}{\left\{1 + \left(\frac{m\lambda}{2nL}\right)^2\right\}}, \quad (23)$$

$$\text{where } \alpha_{2n} = \sqrt{\frac{n\omega\mu_2}{2\rho_2}}.$$

It can be seen that torque is a function of variable \hat{B}_{mn} at some speed because other symbols in (23) are given by mechanical specification.

VI. RESULT AND DISCUSSION

A. Experimental setup

Fig. 9 shows the experimental setup used for the eddy current retarding torque experiments. An engine dynamometer was used to supply the rotational velocity and to measure the retarding torque. A coil current was applied to the retarder from a power supply by a command from a computer, and the retarding torque was recorded in the computer. The rotational velocity was increased from 200 rpm to 1000 rpm. The supplied current was increased from 1 A to 4 A, making a total of 18 A to 72 A when multiplied by the number of poles. In order to exclude the effect of the thermal heat generated at the rotor, the rotor was cooled for more than 30 min. A total of 24 experiments were performed.

B. Comparison between the experimental and theoretical results with the consideration of nonlinear magnetization characteristics of the material

Fig. 10(a) shows the theoretical and experimental results of the torque characteristics of the rotational velocity when the magnetization characteristics are assumed to be linear. When the applied current is low, the theoretical and experimental results agree well. However, when the applied current is increased, the real torque is substantially reduced as compared to the theoretical torque.

Fig. 10(b) shows the theoretical and experimental results for the torque characteristics of the rotational velocity when the magnetization characteristics are nonlinear, since this is practical. As can be seen in the figure, the real torque agrees well with the theoretical torque in the overall current ranges.

C. Dependency of torque characteristics on variations in the design parameter

Fig. 11 shows the torque characteristics with respect to the copper thickness. As shown in Fig. 11(b), the position of the maximum torque varies for different values of d . The torque in a high rotating speed region decreases with an increase in d . This result indicates that the reduction of the magnetic flux from the air gap increases due to increased copper thickness is more dominant than the increase in the eddy current. When the copper thickness increases, the maximum torque is obtained at a low rotational speed.

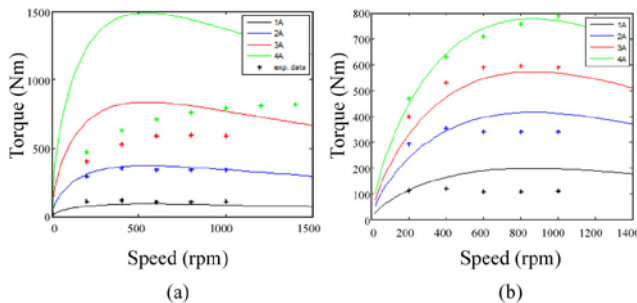


Figure 10. Torque-speed curves for (a) linear model and (b) nonlinear model.

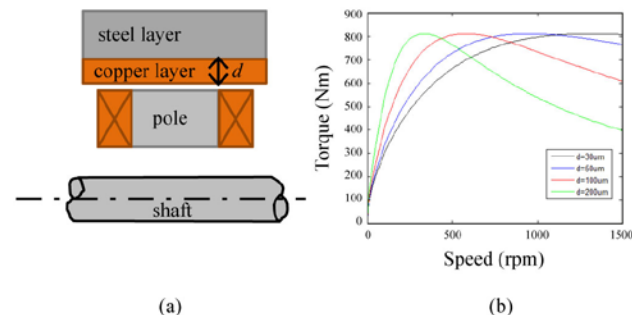


Figure 11. (a) Cross section of the retarder with copper thickness indicated by d and (b) analytical torque curves obtained for $I = 4$ A when d varies by specified values of 30, 50, 100, and 200 μm .

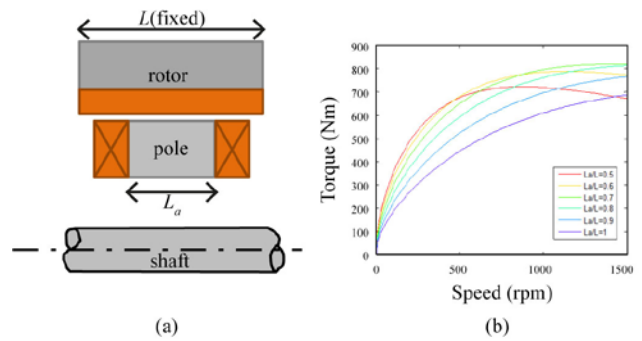


Figure 12. (a) Cross section of the retarder with rotor and pole widths specified as L and L_a , respectively, and (b) analytical torque curves obtained for $I = 4$ A when L_a/L varies from 0.5 to 1.

From these results, it can be said that it is important for the thickness of the copper coating to be evenly distributed over the rotor, since the torque is strongly affected by even a slight variation in its thickness.

Fig. 12 shows how the torque varies with the rotor-width-to-pole-width ratio. In order to compare only the effect of the applied magnetic flux density, the total supplied current and the rotor length were assumed to be constant. As shown in Fig. 12(b), the torque-speed relationship varies for L_a/L .

When the pole area is decreased, even though the magnetic flux density is increased, the torque decreases owing to the reduced area in which the eddy current is generated. For the speed region from 1000 rpm to 1500 rpm, which is a typical driving condition, the ratio of 0.7 gives a maximum torque value.

VII. CONCLUSION

In this paper, we have proposed a process to express the effective magnetic flux in terms of the nonlinear magnetization characteristics of ferromagnetic materials, an issue that has not been considered in previous analytical methods of an ECR. Using a numerical iterative scheme to deal with the nonlinear magnetization relationship, we explained why the torque does not linearly increase in response to higher supplied currents. This result implies that the nonlinearity of the material should be adequately addressed in the analysis of ECRs. Using the iterative analytical model, we discussed the effect of several design parameters on the torque-speed behavior. It was discussed that the copper thickness and the rotor-width-to-pole-width ratio play an important role in determining the torque-speed performance.

For the sake of simple derivation of equations, the rotor surface was assumed to be flat. This assumption would be appropriate if the rotor diameter is much greater than the pole pitch. Further researches on deriving the model based on cylindrical coordinates and comparison it with the model based on Cartesian coordinates would be beneficial for the effect of rotor curvature on the analysis of an ECR.

ACKNOWLEDGMENT

This work was supported by the National Research Foundation of Korea (NRF) grant funded by the Korea government (MEST) (No. 2011-0017876).

REFERENCES

- [1] X. B. Zhao and C. Y. Ji, "Analysis of flux leakage in novel permanent magnet type ECR for vehicle applications," in Vehicle Power and Propulsion Conference, 2008. VPPC '08. IEEE, Sept. 2008, pp. 1-4, doi: 10.1109/VPPC.2008.4677735
- [2] S. M. Jang, S. S. Jeong, and S. D. Cha, "The application of linear Halbach array to eddy current rail brake system," in Magnetics, IEEE Transactions on, vol. 37, July 2001, pp. 2627-2629, doi: . 10.1109/20.951256
- [3] J. S. Choi and J. H. Yoo, "Optimal design method for magnetization directions of a permanent magnet array," Journal of Magnetism and Magnetic Materials, vol. 322, 2010, pp. 2145-2151, doi: 10.1016/j.jmmm.2010.01.047.
- [4] A. B. Dietrich, I. E. Chabu, and J. R. Cardoso, "Eddy-current brake analysis using analytic and FEM calculations. II. Application," Electric Machines and Drives Conference (IEMDC 2001), IEEE International, 2001, pp. 458-461, doi: 10.1109/IEMDC.2001.939344.
- [5] W. R. Smythe, "On Eddy Currents in a Rotating Disk," American Institute of Electrical Engineers, Transactions of the, vol. 294, Sept. 1942, pp. 681-684, doi: 10.1109/T-AIEE.1942.5058590.
- [6] D. Schieber, "Braking torque on rotating sheet in stationary magnetic field," Electrical Engineers, Proceedings of the Institution of, vol. 121, Feb. 1974, pp. 117-122, doi: 10.1049/piee.1974.0021.
- [7] J. H. Wouterse, "Critical torque and speed of eddy current brake with widely separated soft iron poles," Electric Power Applications, IEE Proceedings B, vol. 138, July 1991, pp. 153-158.
- [8] K. J. Lee and K. H. Park, "Analysis of an eddy-current brake considering finite radius and induced magnetic flux," Journal of Applied Physics, vol. 92, Dec. 2001, pp. 5532- 5538, doi: 10.1063/1.1510593.
- [9] E. J. Davies, M. T. Wright, and H. McKibbin, "Three-dimensional theory of eddy-current couplings with copper-faced loss drums," Electrical Engineers, Proceedings of the Institution of, vol. 294, Dec. 1977, pp. 1187-1196, doi: 10.1049/piee.1977.0249.
- [10] M. G. Malti and R. Ramakumar, "Three-Dimensional Theory or the Eddy-Current Coupling," Power Apparatus and Systems, IEEE Transactions on, vol. 82, Oct. 1963, pp. 793-800, doi: 10.1109/TPAS.1963.291410.